Strain induced mobility modulation in single-layer MoS$_2$

Strain induced mobility modulation in single-layer MoS$_2$

Manouchehr Hosseini[1], Mohammad Elahi[1], Mahdi Pourfath[1,2] and David Esseni[3]

[1] School of Electrical and Computer Engineering, University of Tehran, PO Box 14395-515 Tehran, Iran
[2] Institute for Microelectronics, TU Wien, Gusshausstrasse 27–29/E360, 1040 Vienna, Austria
[3] DIEGM, Via delle Scienze 206, 33100 Udine, Italy

E-mail: pourfath@ut.ac.ir, pourfath@iue.tuwien.ac.at and david.esseni@uniud.it

Abstract

In this paper the effect of biaxial and uniaxial strain on the mobility of single-layer MoS$_2$ for temperatures $T > 100$ K is investigated. Scattering from intrinsic phonon modes, remote phonon and charged impurities are considered along with static screening. *Ab initio* simulations are utilized to investigate the strain induced effects on the electronic bandstructure and the linearized Boltzmann transport equation is used to evaluate the low-field mobility under various strain conditions. The results indicate that the mobility increases with tensile biaxial and tensile uniaxial strain along the armchair direction. Under compressive strain, however, the mobility exhibits a non-monotonic behavior when the strain magnitude is varied. In particular, with a relatively small compressive strain of 1% the mobility is reduced by about a factor of two compared to the unstrained condition, but with a larger compressive strain the mobility partly recovers such a degradation.

(Some figures may appear in colour only in the online journal)

I. Introduction

Since the successful experimental isolation of graphene in 2004 [1], ultra-thin two-dimensional structures are being widely studied as potential building blocks for future electronic devices. Graphene exhibits some remarkable electronic properties [2–4], however, the absence of a bandgap has so far precluded its exploitation in electronic applications [5, 6]. Several strategies have been proposed to open a gap, but a band gap larger than 400 meV remains a challenge [5, 7–9]. Other two-dimensional materials with non-zero band gap show promising electronic, optical, and mechanical properties and are considered as potential candidates for future electronic applications [10]. Having a two dimensional structure similar to graphene, transition metal dichalcogenides of the form MX$_2$, where M denotes a transition metal and $X \in \{S, Se, Te\}$, have recently attracted the attention of the scientific community [11, 12]. These materials form layered structures, where layers of covalently bonded X–M–X

groups are held together by Van der Waals interactions [13]. Because of weak inter-layer van der Waals bonds in their layered structure, single to few-layers of these materials can be obtained by mechanical or chemical exfoliation techniques [11, 14, 15].

Out of the transition metal dichalcogenide family, MoS$_2$ is of particular interest [12, 16–18]. A single MoS$_2$ layer is composed of one atomic layer of molybdenum sandwiched between two atomic layers of sulfur and has a total thickness of 0.65 nm (see figure 1). Both theoretical and experimental studies indicate a strong dependency of the band structures on the number of layers [19, 20]. Bulk MoS$_2$ is a semiconductor with an indirect bandgap of 1.2 eV and a carrier mobility in the range of 50–200 cm^2(Vs)$^{-1}$ at room temperature [21]. The bandgap increases as the number of layers is reduced [19, 22]. For a single MoS$_2$ layer a direct bandgap of 1.8–1.9 eV has been reported [12, 17, 21], which makes it suitable for various electronic applications [23]. Recently, field effect transistors based on single-layer MoS$_2$ with an I_{on}/I_{off} ratio as
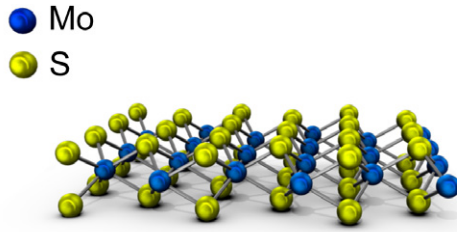
J. Phys. D: Appl. Phys. 48 (2015) 375104

M Hosseini et al

Figure 1. Schematic representation of the atomic structure of single-layer MoS_2.

high as $\sim 10^8$ and a sub-threshold swing of ~ 70 mV/decade have been reported [24–27]. The near ideal sub-threshold swing is due to the strong suppression of short channel effects in low-dimensional materials and excellent electrostatic control of the gate over the channel [28]. Moreover possible applications to hetero-junction inter-layer tunneling FETs have also been proposed and theoretically investigated [29]. Room temperature mobility of n-type single-layer MoS_2 has been reported to be in the range of 0.5–3 cm^2 $(Vs)^{-1}$ and can be increased to about 200 cm^2 $(Vs)^{-1}$ with the use of high-κ dielectrics [25].

The effects of strain on the electronic bandstructure of single-layer MoS_2 have been studied in several works [30, 31]. It has been shown that the application of compressive and tensile biaxial strain results in an indirect band gap in single-layer MoS_2 [32–34]. Even though the low-field mobility is one of the most important transport properties for a large number of physical systems and electronic devices, a comprehensive study of strain effects on the mobility of single-layer MoS_2 has not been reported yet. In the present work, the effects of biaxial and uniaxial strain on the bandstructure and low-field mobility of single-layer MoS_2 is investigated. We employed *ab initio* simulations for calculating the electronic bandstructure parameters for single-layer MoS_2 in the presence of strain. Thereafter, we utilized the linearized Boltzmann transport equation (BTE) that evaluates the low-field mobility without introducing any a priori [35, 36].

In section II some details about the *ab initio* calculations of the electronic bandstructure in the presence of strain are discussed. The formulation of various scattering rates is described in section III. In section IV, the approach for mobility calculation with anisotropic bandstructure and scattering processes is introduced. The effects of different scattering processes on the mobility in the presence of biaxial and uniaxial strain are presented in section V. Finally, concluding remarks are presented in section VI.

II. Bandstructure

We carry out first-principle simulations based on the density-functional theory (DFT) along with the local density approximation (LDA) as implemented in the SIESTA code [37–39] to investigate the relevant electronic properties of a single-layer MoS_2 under strain. While DFT-LDA, in general, underestimates band gaps, the resulting dispersion of individual
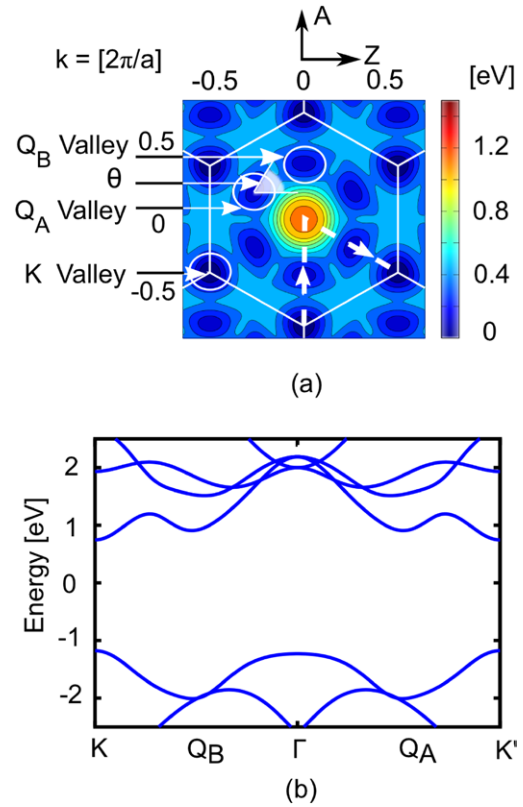

Figure 2. (a) Equi-energy contours in the first Brillouin zone for the unstrained single-layer MoS_2. The angle θ that describes the Q_A valleys orientation in $\vec{k}$-space is also depicted in the figure. It should be recalled that the zigzag direction in $\vec{k}$-space corresponds to the armchair direction in real space. (b) The bandstructure of unstrained single-layer MoS_2 in the first Brillouin zone and along the symmetry directions that are illustrated in (a).

bands, i.e. effective masses and energy differences between the valleys, is less problematic [40]. A cutoff energy equal to 600 Ry is used and a vacuum separation of 30 Å is adopted, which is sufficient to hinder interactions between adjacent layers. Sampling of the reciprocal space Brillouin zone (BZ) is performed by a Monkhorst-Pack grid of $18 \times 18 \times 1$ k-points. Calculations begin with the determination of the optimized geometry, that is the configuration in which the residual Hellmann–Feynman forces acting on atoms are smaller than 0.01 eV Å^{-1}. The calculated lattice constant of unstrained single-layer MoS_2 is 3.11 Å that has a good agreement with the reported value in [22, 41]. Figure 2(a) shows the energy contours of the conduction-band in the first BZ for unstrained single-layer MoS_2. In an unstrained material the lowest and the second lowest minimum in the conduction band are denoted as K and Q-valley, respectively. The 6 K valleys are degenerate in the unstrained and in all the strained conditions explored in this paper. The 6 Q-valleys are degenerate in unstrained conditions, while under uniaxial strain they split into 4 Q_A-valleys and 2 Q_B-valleys with different effective masses and energy minima, as discussed and illustrated in section V. The energy distance between K and Q-valley for unstrained material is evaluated to be 160 meV, in agreement with [40]. Figure 2(b) shows the calculated

DFT-LDA band structure and depicts a direct band gap of 1.92 eV at the K-point which is very close to the experimentally measured value of 1.85 eV [17].

III. Scattering rates

In this section the formulation of scattering with intrinsic phonon, charged impurities, remote phonon, and the screening effects are presented.

III.A. Scattering with MoS$_2$ phonon modes

Scattering rates due to intrinsic phonons (including acoustic, optical and polar-optical phonons), to remote phonons and to charged impurities are taken into account. Piezoelectric coupling to the acoustic phonons is only important at low temperatures and is neglected in this work [42]. If the surrounding dielectric provides a large energy barrier for confining electrons in the MoS$_2$ layer, the envelope function of mobile electrons can be approximated as $\Psi_{\vec{k}}(\vec{r}, z) = \chi(z)\exp(i\vec{k}.\vec{r})/\sqrt{S}$ with $\chi(z) = \sqrt{(2/a)}\sin(\pi z/a)$ [43], where S is the area normalization factor, $\vec{k}$ is the in-plane two-dimensional wave vector, a is the thickness of single-layer MoS$_2$ and $\vec{r}$ is the in-plane position vector. The scattering rates for the acoustic and optical phonon are discussed first.

Using Fermi's golden rule the scattering rate from an initial state $\vec{k}$ in valley v to the final state $\vec{k}'$ in valley w can be written as

$$S^{v,w}(\vec{k}, \vec{k}') = \frac{2\pi}{\hbar}|M^{v,w}(\vec{k}, \vec{k}')|^2 \delta[E^w(\vec{k}') - E^v(\vec{k}) \mp \hbar\omega(q)], \tag{1}$$

where $|M^{v,w}(\vec{k}, \vec{k}')|$ is the matrix element for the mentioned transition and $\hbar\omega(q)$ is the phonon energy that may depend on $q = |\vec{k} - \vec{k}'|$. The intra-valley transitions ($v = w$) assisted by acoustic phonons can be approximated as elastic and the rate is given by

$$S_{ac}(\vec{k}, \vec{k}') = \frac{2\pi k_B T D_{ac}^2}{\rho S \hbar v_s^2}\delta[E(\vec{k}') - E(\vec{k})], \tag{2}$$

where k_B is the Boltzmann constant, T is the absolute temperature, D_{ac} is the acoustic the deformation potential, $\rho = 3.1 \times 10^{-7}$ [gr cm^{-2}] is the mass density and v_s is the sound velocity of single-layer MoS$_2$. On the other hand, the rate of inelastic phonon scattering, including intra and inter-valley optical phonons, and inter-valley acoustic phonons, can be expressed as

$$S_{ac/op}^{v,w}(\vec{k}, \vec{k}') = \frac{\pi(D_{ac/op}^{v,w})^2}{\omega_{ac/op}\rho S}\left[n_{op} + \frac{1}{2} \mp \frac{1}{2}\right]\delta[E^w(\vec{k}') - E^v(\vec{k})$$
$$\mp \hbar\omega_{ac/op}(q)], \tag{3}$$

where $D_{ac/op}^{v,w}$ is the acoustic/optical deformation potential for a transition between valleys v and w, $\hbar\omega_{ac/op}(q)$ is the phonon energy, and n_{op} is the phonon occupation (upper and
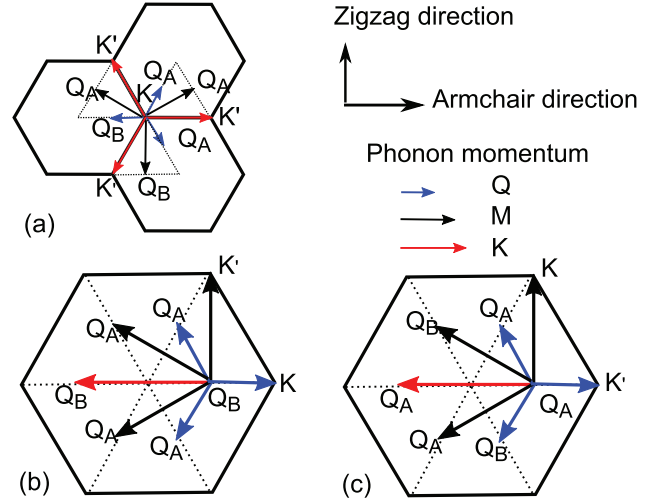

Figure 3. The illustration of several phonon assisted inter-valley transitions in single-layer MoS$_2$ for (a) transitions from K-valley to other valleys; (b) transitions from Q_A-valley to other valleys; (c) transitions from Q_B-valley to other valleys. The figure also sets the notation used in tables 1 and 2 to identify phonon assisted transitions.

lower sign denote phonon absorption and phonon emission, respectively). The phonon assisted inter-valley transitions considered in this work, and the corresponding phonon momentum are shown in figure 3. In our calculations, we employed the deformation potentials and phonon energies from [44] that are reported in tables 1 and 2. It should be noted that the same deformation potentials are used for Q_A and Q_B valleys.

III.B. Remote phonon scattering

Another important scattering source considered in this work is the remote phonon or surface-optical (SO) phonon scattering mechanism. The source of this scattering is in the surrounding dielectrics via long-range Coulomb interactions, provided that the dielectrics support polar vibrational modes. By assuming semi-infinite top and back-oxides and neglecting the possible coupling to the plasmons of the two-dimensional material, the energy dispersion of SO phonons can be obtained by solving the secular equation [45]

$$(\epsilon_{box}(\omega) + \epsilon_{2D})(\epsilon_{tox}(\omega) + \epsilon_{2D}) - (\epsilon_{box}(\omega) - \epsilon_{2D})(\epsilon_{tox}(\omega) - \epsilon_{2D})$$
$$\times e^{-2qa} = 0, \tag{4}$$

where the thickness a of the single-layer MoS$_2$ is set to $a = 3.17$ Å [46], ϵ_{2D} is the dielectric constant of the two-dimensional material (single-layer MoS$_2$ in this work), the indices box and tox denote the back-oxide ($z < 0$) and the top-oxide ($z > a$), respectively, $q = |\vec{k} - \vec{k}'|$ and ϵ_{2D} for MoS$_2$ is set to 7.6 [43]. A numerical solution of equation (4) shows that the frequency of remote phonon has a very weak dependence on q, that consequently we neglected in our calculations by setting $e^{-2qa} \approx 1$ in equation (4). With this approximation, equation (4) simplifies to

Table 1. Deformation potentials for inelastic phonon assisted transitions in single-layer MoS$_2$.

Phonon momentum	Electron transition	Deformation potential
Γ	$K \rightarrow K$	$D_{ac} = 4.5$ eV
Γ	$K \rightarrow K$	$D_{op} = 5.8 \times 10^8$ eV cm^{-1}
K	$K \rightarrow K'$	$D_{ac} = 1.4 \times 10^8$ eV cm^{-1}
K	$K \rightarrow K'$	$D_{op} = 2.0 \times 10^8$ eV cm^{-1}
Q	$K \rightarrow Q$	$D_{ac} = 9.3 \times 10^7$ eV cm^{-1}
Q	$K \rightarrow Q$	$D_{op} = 1.9 \times 10^8$ eV cm^{-1}
M	$K \rightarrow Q$	$D_{ac} = 4.4 \times 10^8$ eV cm^{-1}
M	$K \rightarrow Q$	$D_{op} = 5.6 \times 10^8$ eV cm^{-1}
Γ	$Q \rightarrow Q$	$D_{ac} = 2.8$ eV
Γ	$Q \rightarrow Q$	$D_{op} = 7.1 \times 10^8$ eV cm^{-1}
Q	$Q \rightarrow Q$	$D_{ac} = 2.1 \times 10^8$ eV cm^{-1}
Q	$Q \rightarrow Q$	$D_{op} = 4.8 \times 10^8$ eV cm^{-1}
M	$Q \rightarrow Q$	$D_{ac} = 2.0 \times 10^8$ eV cm^{-1}
M	$Q \rightarrow Q$	$D_{op} = 4.0 \times 10^8$ eV cm^{-1}
K	$Q \rightarrow Q$	$D_{ac} = 4.8 \times 10^8$ eV cm^{-1}
K	$Q \rightarrow Q$	$D_{op} = 6.5 \times 10^8$ eV cm^{-1}
Q	$Q \rightarrow K$ or K'	$D_{ac} = 1.5 \times 10^8$ eV cm^{-1}
Q	$Q \rightarrow K$ or K'	$D_{op} = 2.4 \times 10^8$ eV cm^{-1}
M	$Q \rightarrow K$ or K'	$D_{ac} = 4.4 \times 10^8$ eV cm^{-1}
M	$Q \rightarrow K$ or K'	$D_{op} = 6.6 \times 10^8$ eV cm^{-1}

Note: All parameters are taken from [44].

$\epsilon_{box}(\omega) + \epsilon_{tox}(\omega) = 0$, that we solved by using the single polar phonon expression for the $\epsilon_{ox}(\omega)$ in each oxide:

$$\epsilon_{ox}(\omega) = \epsilon^\infty + \frac{\epsilon^0 - \epsilon^\infty}{1 - \omega^2/\omega_{TO}^2}, \tag{5}$$

where ϵ^∞ and ϵ^0 are the high and low frequency dielectric constants, respectively, and ω_{TO} is the frequency of the polar phonon in the oxide. We could provide analytical solution for equation (5) and express $\omega_{so,box}$ as: $\omega_{so,box}^2 = \left(-B + \sqrt{B^2 - 4AC}\right)/(2A)$ and for $\omega_{so,tox}$ as $\omega_{so,tox}^2 = \left(-B - \sqrt{B^2 - 4AC}\right)/(2A)$, where $A = (\epsilon_{tox}^\infty + \epsilon_{box}^\infty)$, $B = -(\epsilon_{tox}^0 + \epsilon_{box}^\infty) \times \omega_{TO,tox}^2 - (\epsilon_{box}^0 + \epsilon_{tox}^\infty) \times \omega_{TO,box}^2$ and $C = (\epsilon_{tox}^0 + \epsilon_{box}^0) \times \omega_{TO,tox}^2 \times \omega_{TO,box}^2$. Table 3 reports the parameters of dielectric materials that are studied in this work and indicates the corresponding calculated SO phonon frequencies. The scattering matrix element of remote phonon can be written as [45]:

Table 2. The phonon energy for intra-valley and inter-valley transitions at the K, M, and Q points of single-layer MoS$_2$ as reported in [44].

Phonon mode	Γ	K	M	Q
Acoustic [meV]	0	26.1	24.2	20.7
Optical [meV]	49.5	46.8	47.5	48.1

Note: As discussed in [44], the energy values for acoustic (optical) phonon modes are the average of phonon energies of transverse and longitudinal (transverse, longitudinal and homo-polar) modes.

$$M_{so,tox}(\vec{k}, \vec{k}') =$$
$$\sqrt{\frac{\hbar\omega_{so,tox}}{2Sq}\left(\frac{1}{\epsilon_{tox}^\infty + \epsilon_{box}(\omega_{so,tox})} - \frac{1}{\epsilon_{tox}^0 + \epsilon_{box}(\omega_{so,tox})}\right)}, \tag{6}$$

$$M_{so,box}(\vec{k}, \vec{k}') =$$
$$\sqrt{\frac{\hbar\omega_{so,box}}{2Sq}\left(\frac{1}{\epsilon_{box}^\infty + \epsilon_{tox}(\omega_{so,box})} - \frac{1}{\epsilon_{box}^0 + \epsilon_{tox}(\omega_{so,box})}\right)}, \tag{7}$$

scattering with SO phonon mode is inelastic and we consider only intra-valley transitions. The corresponding transition rate is

$$S_{so}(\vec{k}, \vec{k}') = \frac{2\pi}{\hbar}|M_{so}(\vec{k}, \vec{k}')|^2\left[n_{so} + \frac{1}{2} \mp \frac{1}{2}\right]\delta[E(\vec{k}') - E(\vec{k})$$
$$\mp \hbar\omega_{so}], \tag{8}$$

where n_{so} and $\hbar\omega_{so}$ are the SO phonon occupation number and energy, respectively.

III.C. Scattering with coulomb centers

To investigate the effect of the dielectric environment on the scattering of carriers from charged impurities located inside the single-layer MoS$_2$, we assume that the charged impurities are located in the center of the single-layer MoS$_2$ thickness, that is at $z = a/2$. The Fourier transform of the scattering potential due to a charged impurity located at $(\vec{r}, z) = (0, a/2)$ can be written as [47]

$$\phi(q, z) = \frac{e^2}{2q\epsilon_{2D}}[e^{-q|z-a/2|} + Ce^{qz} + De^{-qz}], \tag{9}$$

where e is the elementary charge, and C and D can be written as

$$C = \frac{(\epsilon_{2D} - \epsilon_{box}^0)(\epsilon_{2D} - \epsilon_{tox}^0)e^{-qa/2} + (\epsilon_{2D} + \epsilon_{box}^0)(\epsilon_{2D} - \epsilon_{tox}^0)e^{aq/2} - (\epsilon_{box}^0 - \epsilon_{2D})(\epsilon_{tox}^0 + \epsilon_{2D})}{(\epsilon_{2D} + \epsilon_{box}^0)(\epsilon_{2D} + \epsilon_{tox}^0)e^{2aq} - (\epsilon_{2D} - \epsilon_{box}^0)(\epsilon_{2D} - \epsilon_{tox}^0)}, \tag{10}$$

J. Phys. D: Appl. Phys. **48** (2015) 375104

M Hosseini *et al*

Table 3. Parameters for the top-oxide dielectric materials taken from (a) [52] and (b) [53] and corresponding calculated SO phonon frequencies $\hbar\omega_{so,tox}$ and $\hbar\omega_{so,box}$.

Material	$SiO_2^{(a)}$	$BN^{(b)}$	$AlN^{(a)}$	$Al_2O_3^{(a)}$	$HfO_2^{(a)}$	$ZrO_2^{(a)}$
ϵ_{tox}^0	3.9	5.09	9.14	12.53	23	24
ϵ_{tox}^∞	2.5	4.1	4.8	3.2	5.03	4
$\omega_{TO,tox}$ [meV]	55.6	93.07	81.4	48.18	12.4	16.67
$\omega_{so,tox}$ [meV] (Evaluated in this work)	69.4	100.5	104.3	83.9	21.3	30.5
$\omega_{so,box}$ [meV] (Evaluated in this work)	69.4	60.1	58.0	54.2	61.1	62.9

Note: In all of the cases back-oxide is assumed to be SiO_2.

and

$$D = \frac{(\epsilon_{box}^0 - \epsilon_{2D})[C + e^{-qa/2}]}{\epsilon_{box}^0 + \epsilon_{2D}}. \tag{11}$$

Using equation (9), the $\chi(z)$ form $\chi(z) = \sqrt{(2/a)}\sin(\pi z/a)$ and assuming intra-valley transitions for scattering with charged impurities, the transition matrix elements take the form

$$M_{cb}^{(0)}(\vec{k}, \vec{k}') = \frac{e^2}{qa\epsilon_{2D}}\left(\frac{1}{q} - \frac{q}{q^2 + (2\pi/a)^2}\right)$$
$$\times \left[\frac{C}{2}(e^{qa} - 1) + \frac{D}{2}(1 - e^{-qa}) - e^{-qa/2}\right] \tag{12}$$
$$+ \frac{e^2}{qa\epsilon_{2D}}\left(\frac{1}{q} + \frac{q}{q^2 + (2\pi/a)^2}\right),$$

where $q = |\vec{k} - \vec{k}'|$. Equation (12) expresses the matrix element for a Coulomb center located in $(\vec{r}, z) = (0, a/2)$ and does not account for the screening produced by the free carriers in MoS_2; such a screening effect is introduced according to the dielectric matrix approach discussed in section III.D. The overall matrix element produced by a set of Coulomb centers randomly distributed at positions $(\vec{r}, a/2)$ is known to be affected by the statistical properties of the distribution and, in particular, by a possible correlation between the position of Coulomb centers. In this paper we do not address these difficulties and simply write the overall matrix element as $|M_{cb}(\vec{k}, \vec{k}')|^2 = [N_D|M_{cb}^{(0)}(\vec{k}, \vec{k}')|^2]/S$, where N_D is the impurity density per unit area and $M_{cb}^{(0)}$ is given by equation (12). Scattering charged impurities is treated as elastic and the rate is therefore given by

$$S_{cb}(\vec{k}, \vec{k}') = \frac{2\pi}{\hbar}|M_{cb}(\vec{k}, \vec{k}')|^2\delta(E(\vec{k}') - E(\vec{k})). \tag{13}$$

III.D. Screening

The effect of static screening produced by the electrons in the MoS_2 conduction band is described by using the dielectric function approach [47], so that the screened matrix element $M_{scr}^w(\vec{k}, \vec{k}')$ of the valley w is obtained by solving the linear problem:

$$M^v(q) = \sum_w \epsilon^{v,w}(q)M_{scr}^w(q), \tag{14}$$

where $M^v(q)$ are the unscreened matrix element. As can be seen in figure 2(a), there are three different valleys in strained single-layer MoS_2 (K, Q_A and Q_B valleys), hence v, $w \in \{K, Q_A, Q_B\}$. In equation (14), $\epsilon^{v,w}$ is the dielectric matrix which is introduced as:

$$\epsilon^{v,w}(q) = \delta_{v,w} - \frac{e^2}{q(\epsilon_{2D} + \epsilon_{box})}\Pi^w(q)F^{v,w}(q), \tag{15}$$

where $\delta_{v,w}$ is the Kronecker symbol (1 if $v = w$, otherwise zero), $\Pi^w(q)$ and $F^{v,w}(q)$ are the polarization factor and unit-less screening form factor, respectively [47]. In the case at study the dielectric matrix can be analytically inverted to evaluate screened matrix elements as:

$$M_{scr}^v(q) = \frac{\left(1 - \sum_{w \neq v}\epsilon^{v,w}(q)\right)M^v(q) + \sum_{w \neq v}\epsilon^{v,w}(q)M^w(q)}{2 - \sum_w\epsilon^{v,w}(q)}. \tag{16}$$

The static dielectric function approach described above has been directly used for the scattering due to charged impurities, while the situation is admittedly more complicated for phonon scattering. For the inelastic, inter-valley phonon transitions described in tables 1 and 2 the relatively large phonon wave-vector (see also figure 3) and the non-null phonon energies suggest that it is safe to leave these transitions unscreened, because the dynamic descreening and the large phonon wave-vectors make the screening very ineffective. Arguments concerning screening for intra-valley acoustic phonons are more subtle and controversial and a thorough discussion for inversion layer systems can be found in [48]. We here decided to leave also intra-valley acoustic phonons unscreened, which is the choice employed in essentially all the studies concerning transport in inversion layers that the authors are aware of. The screening of the SO phonon scattering is also a delicate subject, because the polar phonon modes of the high-κ dielectrics can couple with the collective excitations of the electrons in the MoS_2 layer and thus produce coupled phonon-plasmon modes [45, 48], whose treatment is further complicated by the possible occurrence of Landau damping [45, 48, 49]. In this paper we do not attempt a full treatment of the coupled phonon-plasmon modes [45, 48], but instead show in in section V results for the two extreme cases of either unscreened SO phonons or SO phonons screened according to the static dielectric function. We can anticipate that while the inclusion of static screening in SO phonons implies a significant mobility enhancement compared to the unscreened case, the

mobility dependence on the strain and on the dielectric constant of the high-κ dielectrics is not significantly affected by the treatment of screening for SO phonons.

IV. Mobility calculation

Acoustic, optical, polar-optical, remote phonon, and charged impurity scatterings are considered for the calculation of low-field mobility. As it will be discussed in the next section, the bandstructure for Q_A and Q_B valleys is not isotropic and the mobility shows direction-dependence, hence we calculated mobility by solving numerically the linearized Boltzmann transport equation (BTE) according to the approach described in [35], which does not introduce any simplifying assumption in the BTE solution. In particular, mobility has been calculated along the armchair and zigzag directions and strain has been also studied for the uniaxial configuration along either armchair or zigzag direction, as well as for the biaxial configuration.

In order to describe in more detail the mobility calculation procedure, we first recall that the longitudinal direction of Q_A-valley is neither the armchair nor the zigzag direction, and figure 2(a) shows that θ is the angle describing the valley orientation with respect to the zigzag direction in k-space (i.l. armchair direction in real space). Let us now consider first the case of the mobility $\mu_A^{(v)}$ of valley v along the armchair direction, that can be written by definition as $\mu_A^{(v)} = J_A^{(v)}/F_A$, where $J_A^{(v)}$ is the current component in the armchair direction for the valley v induced by the electric field F_A along armchair direction. The current $J_A^{(v)}$ can be expressed as $J_A^{(v)} = J_l^{(v)}\cos(\theta_v) + J_t^{(v)}\sin(\theta_v)$ in terms of the current components $J_l^{(v)}$, $J_t^{(v)}$ along, respectively, the longitudinal and transverse direction of the valley v. By denoting the longitudinal (F_l) and transverse component (F_t) of the electric field as $F_l = F_A\cos(\theta_v)$ and $F_t = F_A\sin(\theta_v)$, the currents $J_l^{(v)}$ and $J_t^{(v)}$ in turn can be written as $J_l^{(v)} = \mu_{ll}^{(v)}F_l + \mu_{lt}^{(v)}F_t$ and $J_t^{(v)} = \mu_{lt}^{(v)}F_l + \mu_{tt}^{(v)}F_t$, where μ_{ll}, μ_{tt} and μ_{lt} are the entries of the two by two mobility matrix in the valley coordinate system [47]. Consequently we finally obtain:

$$\mu_A^{(v)} = \frac{J_A^{(v)}}{F_A} = \mu_{ll}^{(v)}\cos^2(\theta_v) + \mu_{tt}^{(v)}\sin^2(\theta_v) + 2\mu_{lt}^{(v)}\sin(\theta_v)\cos(\theta_v). \tag{17}$$

By following a similar procedure, the mobility $\mu_Z^{(v)}$ of the valley v along the zigzag direction can be written as:

$$\mu_Z^{(v)} = \frac{J_Z^{(v)}}{F_Z} = \mu_{ll}^{(v)}\sin^2(\theta_v) + \mu_{tt}^{(v)}\cos^2(\theta_v) - 2\mu_{lt}^{(v)}\sin(\theta_v)\cos(\theta_v). \tag{18}$$

For the circular and elliptical bands employed in our calculations (see figure 4(g)), $\mu_{lt}^{(v)}$ is zero for symmetry reasons [47]. After calculating the mobility for each valley, the overall mobilities μ_A and μ_Z are obtained as the average of the mobility in the different valleys weighted by the corresponding electron density.

Equations (17) and (18) allow us to calculate the mobility $\mu_A^{(v)}$ and $\mu_Z^{(v)}$ from the longitudinal μ_{ll}^v and the transverse

mobility μ_{tt}^v of the valley v which are the mobilities obtained from the linearized BTE when the electric field is either in the longitudinal or in the transverse direction of the valley v. As already said, the μ_{ll}^v and μ_{tt}^v have been obtained by using the approach of [35], whose derivation for the case at study in this work can be summarized as follows. The out of equilibrium occupation function $f^v(\vec{k})$ for the valley v in the presence of a field F_x is written as

$$f^v(\vec{k}) = f_0(E^v(\vec{k})) - eF_x g^v(\vec{k}), \tag{19}$$

where $f_0(E)$ is the equilibrium Fermi–Dirac distribution function, $x \in \{l, t\}$ is either the longitudinal or the transverse direction of the valley and $\vec{k} = (k_l, k_t)$ is the wavevector in the valley coordinate system. Equation (19) is a definition of $g^v(\vec{k})$, which is the unknown function of the linearized BTE problem. For a two-dimensional system the linearized BTE can be written as [35]

$$g^v(\vec{k})\left(\frac{1}{2\pi\hbar}\sum_w\int_{\vec{k}'}\Gamma^{v,w}(\vec{k},\vec{k}')\delta[E^w(\vec{k}') - E^v(\vec{k}) \mp \hbar\omega_{ph}]\,d\vec{k}'\right)$$
$$-\frac{1}{2\pi\hbar}\sum_w\int_{\vec{k}'}\Lambda^{v,w}(\vec{k},\vec{k}')g^w(\vec{k}')\delta[E^w(\vec{k}') - E^v(\vec{k}) \mp \hbar\omega]d\vec{k}'$$
$$= v_x^v(\vec{k})\frac{(f_0(E^v(\vec{k})))(1 - f_0(E^v(\vec{k})))}{k_B T}, \tag{20}$$

where v_x^v is the x component of the group velocity of valley v and, for convenience of notation, we have introduced the quantities

$$\Gamma^{v,w}(\vec{k},\vec{k}') = |M^{v,w}(\vec{k},\vec{k}')|^2\left[\frac{1 - f_0(E^w(\vec{k}'))}{1 - f_0(E^v(\vec{k}))}\right]$$
$$\Lambda^{v,w}(\vec{k},\vec{k}') = |M^{v,w}(\vec{k},\vec{k}')|^2\left[\frac{f_0(E^v(\vec{k}))}{f_0(E^w(\vec{k}'))}\right] \tag{21}$$

To numerically solve equation (20), we employed the discretization scheme introduced in [35]: $\vec{k}$ is discretized according to a uniform angular step $\Delta\beta$ and also a uniform energy step. The discrete values $k_{v,r,d}$ of the wave-vector magnitude correspond to one of the discrete energy values and the generic discrete wave-vector $\vec{k}_{v,r,d} = (k_{v,r,d}, d\Delta\beta)$ is identified by the magnitude $k_{v,r,d}$ and the angle $d\Delta\beta$ (with d being a positive integer number). For each scattering mechanism, by converting the integral over $\vec{k}$ in an integral over the energy and the angle β and then using the above mentioned discretization, equation (20) can be rewritten as:

$$g(k_{v,r,d})\left[\frac{\Delta\beta}{2\pi\hbar}\sum_{w,r',d'}A_{v,r,d}^{w,r',d'}\delta_{v,r,d}^{w,r',d'}\right] - \frac{\Delta\beta}{2\pi\hbar}\sum_{w,r',d'}B_{v,r,d}^{w,r',d'}g(k_{w,r',d'})\delta_{v,r,d}^{w,r',d'}$$
$$= \frac{v_x(k_{v,r,d})f_0(E(k_{v,r,d}))[1 - f_0(E(k_{v,r,d}))]}{k_B T}. \tag{22}$$

Equation (22) is a linear problem for the discretized unknown values $g(k_{v,r,d})$ written in terms of the coefficients $A_{v,r,d}^{w,r',d'}$ and $B_{v,r,d}^{w,r',d'}$ defined as
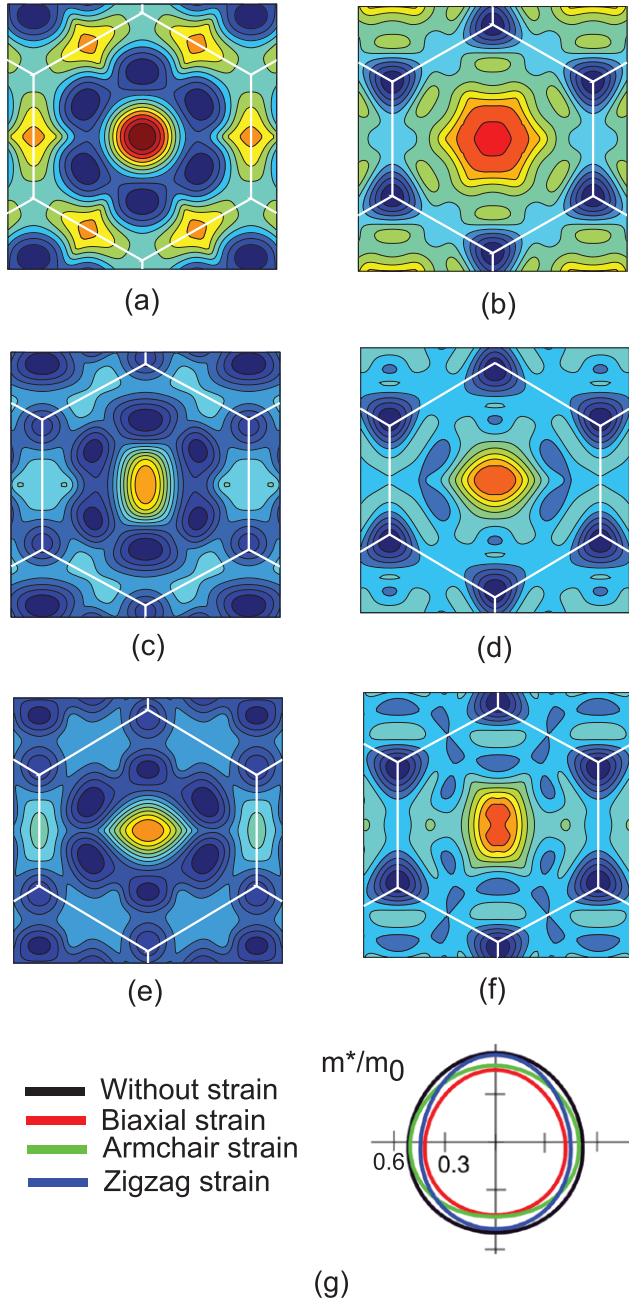
Figure 5. The band structure of unstrained and strained single-layer MoS_2. BI: biaxial strain, UA: uniaxial strain along armchair direction; UZ: uniaxial strain along zigzag direction. The strain magnitude is 4% in all strained cases.

$$B_{v,r,d}^{w,r',d'} = \frac{k_{w,r',d'} \times |M^{v,w}(k_{v,r,d}, k_{w,r',d'})|^2}{\left(\frac{dE(k_{w,r',d'})}{dk}\right)} \left[\frac{f_0(E(k_{v,r,d}))}{f_0(E(k_{w,r',d'}))}\right],$$

(24)

where the non-zero entries of the matrix representing the linear problem are governed by the Kronecker symbols $\delta_{v,r,d}^{w,r',d'}$, that are defined so to enforce energy conservation [35].

Equation (22) has been written for a single scattering mechanism. In order to accommodate several scattering mechanisms in our calculations, we do not resort to an approximated treatment based on the Matthiessen rule [50], but instead follow [35] and notice that equation (22) can be written in the concise matrix notation $\bar{\bar{M}}^{(s)}\bar{g} = \bar{G}$, where $\bar{\bar{M}}^{(s)}$ is a matrix specific of the scattering mechanisms s, $\bar{g}$ is the unknown vector and $\bar{G}$ is the vector at the right hand side of equation (22) and consisting of known quantities. Hence the unknown vector $\bar{g}$ corresponding to several scattering mechanisms can be obtained by solving the linear problem

$$\left[\sum_{s=1}^{N_{SC}} \bar{\bar{M}}^{(s)}\right]\bar{g} = \bar{G},$$

(25)

where equation (22)–(24) will totally define the entries of the matrix $\bar{\bar{M}}^{(s)}$ for each scattering mechanism.

V. Results and discussions

Figure 4 shows the energy contours of the conduction-band in the first BZ for strained single-layer MoS_2. In an unstrained material the lowest and the second lowest minimum in the conduction band are denoted as K-valley and Q-valley, respectively. The 6 Q-valleys are degenerate for unstrained and biaxial strain conditions. With the application of uniaxial strain, however, they split into 4 Q_A-valleys and 2 Q_B-valleys with different effective masses and energy minima. Figure 5 illustrates the bandstructure of unstrained and strained single-layer MoS_2 including K, Q_A, and Q_B valleys. Under compressive strain one of the Q_A or Q_B valleys becomes the lowest valley.

(a)   (b)   (c)   (d)   (e)   (f)

m*/m₀

0.6   0.3

(g)

Without strain
Biaxial strain
Armchair strain
Zigzag strain

Figure 4. Equi-energy contours for single-layer MoS_2 under: (a) compressive biaxial strain; (b) tensile biaxial strain; (c) compressive uniaxial strain along the armchair direction; (d) tensile uniaxial strain along the armchair direction; (e) compressive uniaxial strain along the zigzag direction; (f) tensile uniaxial strain along the zigzag direction. (g) Extracted effective mass of K-valley along all directions in polar coordinate for unstrained MoS_2 and under tensile biaxial and uniaxial strain along armchair and zigzag directions. The nearly circular shape of the effective mass plot justifies the assumption of isotropic bandstructure. The strain magnitude is 4% in all strained cases. The longitudinal and transverse effective masses of Q-valleys vary with the strain conditions.

$$A_{v,r,d}^{w,r',d'} = \frac{k_{w,r',d'} \times |M^{v,w}(k_{v,r,d}, k_{w,r',d'})|^2}{\left(\frac{dE(k_{w,r',d'})}{dk}\right)} \left[\frac{1 - f_0(E(k_{w,r',d'}))}{1 - f_0(E(k_{v,r,d}))}\right],$$

(23)

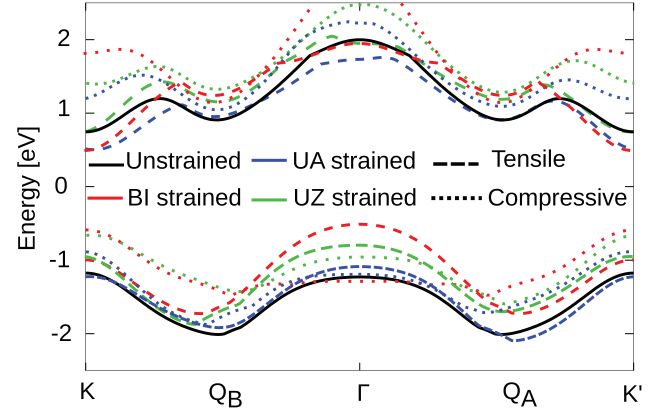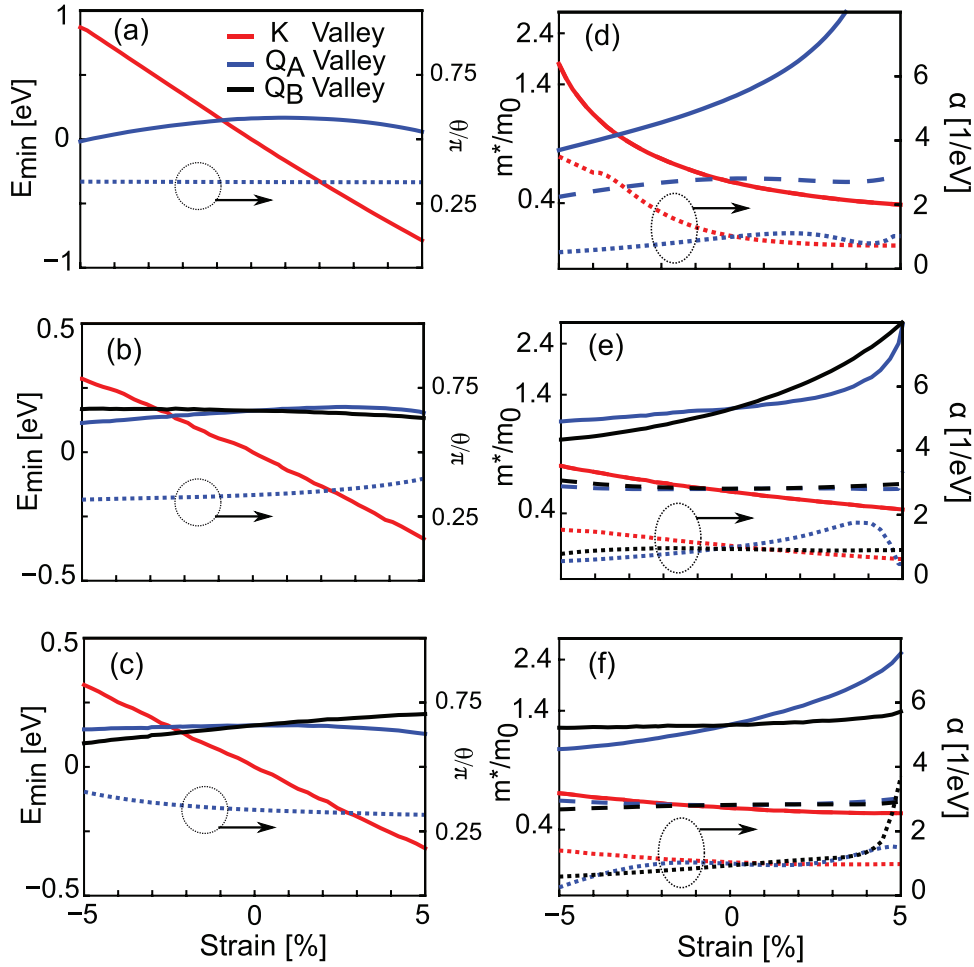**Figure 6.** The energy minima of valleys (solid-lines) and the angle θ (dotted lines) between the longitudinal direction of Q_A valleys and zigzag direction in k-space as illustrated in figure 2(a) under: (a) biaxial strain; (b) uniaxial strain along the armchair direction; (c) uniaxial strain along the zigzag direction. The θ angle in figures 6(a)–(c) corresponds to the Q_A valley indicated in figure 2(a), and the θ angle of the other Q_A valleys can be inferred from symmetry considerations. The θ angle for Q_B valleys has a negligible dependence on strain (not shown) and it is approximately zero (see figure 2(a)). The effective masses (solid-lines for longitudinal and dashed-lines for transverse) and the non-parabolicity factors (α) (dotted-lines) of various valleys under: (d) biaxial strain; (e) uniaxial strain along the armchair direction; (f) uniaxial strain along the zigzag direction. The longitudinal and transverse effective masses of K-valley are assumed to be equal.

The energy distance between these K-valley and Q-valley for unstrained material is evaluated to be 160 meV, in agreement with [40]. A tensile strain increases this energy distance, which is instead reduced by a compressive strain. In particularly, a relatively large compressive strain lowers the energy of Q-valley so that it becomes the lowest valley as shown in figures 6(a)–(c). Here we can anticipate that, while under tensile strain one can neglect the scattering between Q and K-valleys, under compressive strain this type of scattering can significantly affect the mobility. Assuming a non-parabolic dispersion relation $E(1 + \alpha E) = \hbar^2 k_l^2/2m_l^* + \hbar^2 k_t^2/2m_t^*$, the longitudinal m_l^* and transverse m_t^* effective mass and also the non-parabolicity factor α are extracted from the DFT-calculated electronic bandstructure and reported in figures 6(d)–(f). As can be seen in figures 6(a)–(c), under compressive uniaxial strain the energy minima of all K- and Q-valleys are quite close, while at large compressive biaxial strain the K-valley lie at higher energy and their contribution to mobility can be neglected.

We compare in table 4 our calculated mobilities at various carrier concentrations with the experimental data reported

in [51] for unstrained single-layer MoS$_2$ embedded between SiO$_2$ and HfO$_2$ with impurity density 4×10^{12}. At $T = 100$ K the effect of piezoelectric can be ignored [42]. Very good agreement with experimental data validates the bandstructure and mobility models employed in this work.

The strain-dependency of the intrinsic phonon limited mobility is presented in figure 7(a). Apparently, the effects of compressive and tensile strain on mobility are very different, which can be mainly explained by considering the role of inter-valley scattering. For example, with tensile strain the minimum energies of Q_A and Q_B-valleys are much higher than that of K-valley, which suppresses inter-valley scattering. Under compressive strain, instead, the inter-valley scattering cannot be neglected because of the smaller energy difference between these valleys. With tensile biaxial strain, the mobility increases because of the reduction of the effective mass and also the increase of the energy difference between K and Q-valleys, which results in the reduction of the inter-valley scattering rate. With a tensile biaxial strain of 5% the phonon limited mobility becomes 75% higher than that of

Table 4. The comparison of the calculated mobility (μ) in this work with the experimental data of [51] at various carrier concentrations (n).

Carrier concentration [cm^{-2}]	7.6×10^{12}	9.6×10^{12}	1.15×10^{13}	1.35×10^{13}
Calculated mobility, this work [cm^2 (Vs)$^{-1}$]	93	106	114	122
Experimental mobility [cm^2 (Vs)$^{-1}$]	96 ± 3	111 ± 3	128 ± 3	132 ± 3

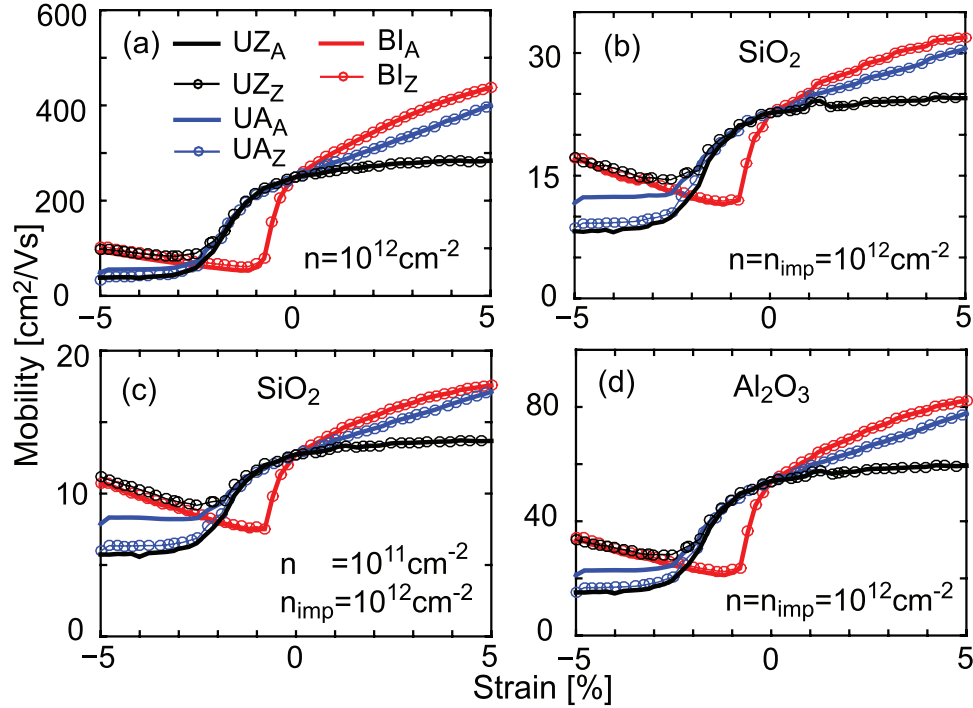*Note*: $T = 100$ K and the impurity density is equal to 4×10^{12} cm^{-2}.

Figure 7. (a) The phonon limited mobility of single-layer MoS$_2$ as a function of strain with a carrier concentration $n = 10^{12}$ cm^{-2}. The mobility limited by phonon and screened charged impurity scattering with SiO$_2$ as the gate oxide ($\epsilon_r = 3.9$) and carrier (n) and charged impurity concentration (n_{imp}) for: (b) $n = n_{imp} = 10^{12}$ cm^{-2}; (c) $n = 10^{11}$ cm^{-2} and $n_{imp} = 10^{12}$ cm^{-2}. (d) Same as (b), except for the top-oxide which is Al$_2$O$_3$. In the legend, BI, UA, and UZ denote a biaxial strain, a uniaxial strain along the armchair direction, and a uniaxial strain along the zigzag direction respectively. The subscripts A and Z indicate the component of the mobility along the armchair or zigzag direction. For example: UZ$_A$ is the mobility along the armchair direction for a uniaxial strain along zigzag direction.

unstrained material. In contrast, a compressive biaxial strain of 0.8% strongly reduces the mobility due to the reduction of energy difference between K and Q-valleys (see figure 6(a)) and increased inter-valley scattering. With further increase of compressive biaxial strain, Q-valleys become the lowest ones and thus dominate the mobility. At a strain value of about 2.5% the contribution of K-valleys to mobility becomes negligible and the mobility behavior is completely determined by the Q-valleys. Longitudinal and transverse effective masses of Q-valleys are not equal and are somewhat changed by strain, however, the different angular dependency of mobility along the armchair and zigzag direction tends to compensate the changes of effective masses and the overall mobility remains nearly constant at larger compressive strain values.

Under tensile uniaxial strain the mobility is hardly affected by a strain along the zigzag direction, while it increases for strain along the armchair direction. In both cases the variation of the effective mass and non-parabolicity factor with strain determine the mobility behavior. Under a compressive uniaxial strain along the armchair direction, Q_A becomes the lowest valley, while for a strain along the zigzag direction Q_B is the lowest one. These

results emphasize that the contribution of both Q_A and Q_B valley should be included for an accurate calculation of mobility. Under a compressive strain of about 1.5% the mobilities are strongly reduced, but they remain nearly constant for larger strain magnitudes. Moreover, we notice that for a strain along the zigzag direction, the mobility along the strain direction becomes slightly larger than the mobility in the armchair direction.

Figure 7(b) reports the mobility in the presence of intrinsic phonon and charged impurity scattering. The top and bottom oxide are assumed to be SiO$_2$ and both carrier and impurity concentrations are 10^{12} cm^{-2}. Except for a global reduction of the mobility, the behavior of the mobility with strain is similar to figure 7(a) corresponding to the phonon limited mobility. The results presented in figure 7(c) correspond to the same parameters as in figure 7(b), except for a reduction of carrier concentration to 10^{11} cm^{-2}. As the carrier concentration decreases the effect of static screening becomes weaker and the mobility is further reduced. Figure 7(d) illustrates the mobility as a function of strain with the same parameters used in figure 7(b), expect for the top and bottom gate oxide which is Al$_2$O$_3$. A high-κ dielectric implies a larger dielectric screening

J. Phys. D: Appl. Phys. 48 (2015) 375104
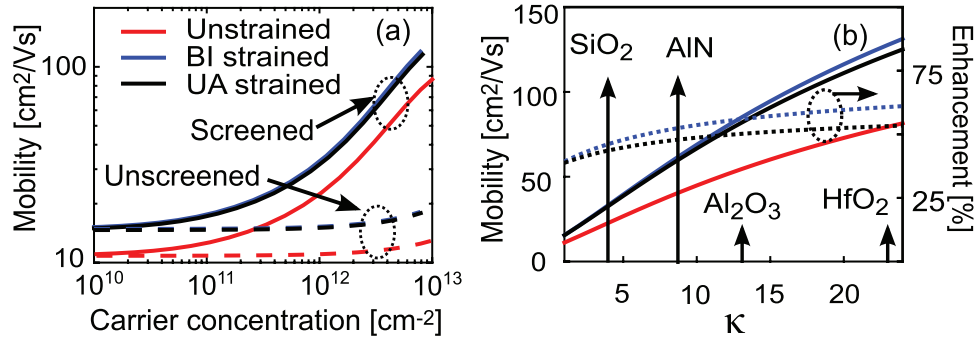
M Hosseini *et al*

Figure 8. (a) The mobility versus carrier concentration with and without screening for the unstrained MoS₂, for a tensile biaxial strain of 5%, and for a uniaxial strain of 5% along the armchair direction. $n_{imp} = 10^{12}$ cm^{-2}. (b) The mobility versus the relative dielectric constant for unstrained MoS₂ and for strain conditions as in (a). $n = n_{imp} = 10^{12}$ cm^{-2}. The strain induced mobility enhancement is shown on the right-side of the *y*-axis.
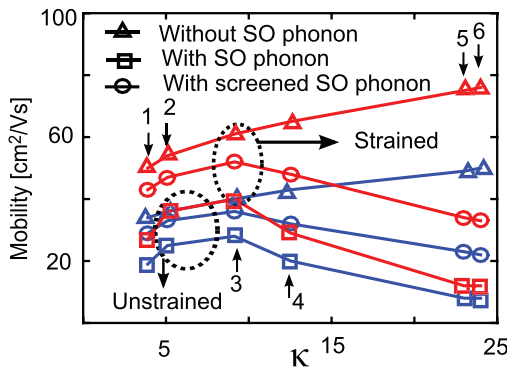

Figure 9. The mobility accounting for intrinsic phonon and charged impurity scattering (triangle), and for either unscreened (rectangle) or screened (circle) SO phonon scattering as a function of top oxide dielectric constant for unstrained (blue line) and 5% biaxial strain (red line). Numbers 1–6 indicate the κ value corresponding to dielectric materials studied in this work (see also table 3). In particular, (1): SiO₂, (2): BN, (3): AlN, (4): Al₂O₃, (5): HfO₂, and (6): ZrO₂. In all cases the back oxide is assumed to be SiO₂. $T = 300$ K, the impurity and carrier concentrations are equal to 4×10^{12} cm^{-2} and 10^{13} cm^{-2}, respectively. These values are consistent with experimental data reported in [51].

and increases the mobility. Under this condition, with a tensile biaxial strain of 5% and a tensile uniaxial strain of 5% along the armchair direction the mobility increases by 53% and 43%, respectively, compared to an unstrained single-layer MoS₂. For a better comparison, figure 8 shows the room temperature mobility versus carrier concentration and also versus the dielectric constant for the unstrained material and for 5% tensile strain in either a biaxial or a uniaxial configuration along the armchair direction with an impurity density equal to 10^{12} cm^{-2}. As can be seen in figure 8(a), because of screening the mobility increases with the carrier concentration for both unstrained and strained cases. Figure 8(b) indicates that the strain induced mobility enhancement with high-κ dielectric materials is slightly larger than that with low-κ materials.

The effect of unscreened and screened remote phonon scattering on the mobility of unstrained and 5% biaxial strained single-layer MoS₂ are compared in figure 9. Except for a global increase of mobility values. The mobility dependence on the dielectric constant κ is not significantly affected by the screening of SO phonons. As can be seen, for relatively
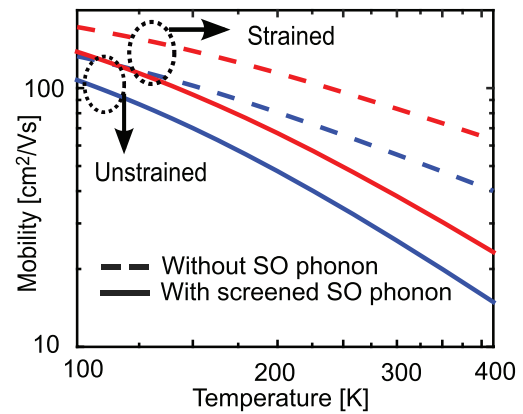

Figure 10. The mobility with the inclusion of intrinsic phonon and charged impurity scattering (dash line) and with the inclusion of screened SO phonon (solid line) versus temperature for a SiO₂/MoS₂/HfO₂ structure for unstrained (blue line) and 5% biaxial strain (red line). The impurity and carrier concentrations are equal to 4×10^{12} cm^{-2} and 10^{13} cm^{-2}, respectively.

small κ values, mobility improves with increasing κ because of the dielectric screening of charged impurities [43]. At high κ values, however, the mobility decrease with increasing κ because the corresponding smaller SO phonon energies (see table 3) tend to increase momentum relaxation time via SO phonons. For the conditions considered in figure 9 (temperature, carrier and impurity concentrations, and semi-infinite dielectrics with SiO₂ as the bottom oxide), AlN appears to be the optimal top dielectric material for strained and also unstrained single-layer MoS₂. Figure 10 shows the temperature dependency of the mobility for unstrained and 5% biaxial strain with HfO₂ as the top oxide. As expected the effect of inelastic remote phonons increases with temperature for both unstrained and strained cases. Therefore, it is expected that the optimal material as a top dielectric for temperatures above (bellow) 300 K, should have a lower(higher)-κ compared to AlN.

VI. Conclusion

A comprehensive theoretical study on the role of strain on the mobility of single-layer MoS₂ is presented. DFT calculations

J. Phys. D: Appl. Phys. 48 (2015) 375104

M Hosseini *et al*

are used to obtain the effective masses and energy minima of the contributing valleys. Thereafter, the linearized BTE is solved for evaluating the mobility, including the effect of intrinsic phonons, remote phonons, and screened charged impurities. The results indicate that, a tensile strain increases the mobility, while compressive strain reduces the mobility. Furthermore, biaxial strain and uniaxial strain along the armchair direction increase the mobility more effectively. The strain-dependency of the mobility of MoS_2 is rather complicated and strongly depends on the relative positions of Q and K-valleys and the corresponding inter-valley scattering. The presented results pave the way for a possible strain engineering of the electronic transport in MoS_2 based electron devices and the awareness of the quite critical mobility dependence on strain may also prove useful in the interpretation of the electron mobility experimental data in single-layer MoS_2 transistors.

Acknowledgments

References

[1] Novoselov K S, Geim A K, Morozov S, Jiang D, Zhang Y, Dubonos S, Grigorieva I and Firsov A 2004 *Science* **306** 666–9

[2] Lin Y M, Dimitrakopoulos C, Jenkins K A, Farmer D B, Chiu H Y, Grill A and Avouris P 2010 *Science* **327** 662

[3] Wang H W H, Nezich D, Kong J K J and Palacios T 2009 *IEEE Electron Device Lett.* **30** 547–9

[4] Dean C *et al* 2010 *Nat. Nanotechnol.* **5** 722–6

[5] Zhang Y, Tang T T, Girit C, Hao Z, Martin M C, Zettl A, Crommie M F, Shen Y R and Wang F 2009 *Nature* **459** 820–3

[6] Gava P, Lazzeri M, Saitta A M and Mauri F 2009 *Phys. Rev. B* **79** 165431

[7] Son Y W, Cohen M L and Louie S G 2006 *Phy. Rev. Lett.* **97** 216803

[8] Giovannetti G, Khomyakov P A, Brocks G, Kelly P J and van den Brink J 2007 *Phys. Rev. B* **76** 073103

[9] Han M Y, Özyilmaz B, Zhang Y and Kim P 2007 *Phys. Rev. Lett.* **98** 206805

[10] Neto A and Novoselov K 2011 *Rep. Prog. Phys.* **74** 82501–9

[11] Novoselov K, Jiang D, Schedin F, Booth T, Khotkevich V, Morozov S and Geim A 2005 *Proc. Natl Acad. Sci.* **102** 10451–3

[12] Mak K F, Lee C, Hone J, Shan J and Heinz T F 2010 *Phys. Rev. Lett.* **105** 136805

[13] Wilson J and Yoffe A 1969 *Adv. Phys.* **18** 193–335

[14] Ayari A, Cobas E, Ogundadegbe O and Fuhrer M S 2007 *J. Appl. Phys.* **101** 014507

[15] Matte H R, Gomathi A, Manna A K, Late D J, Datta R, Pati S K and Rao C 2010 *Angew. Chem. Int. Ed.* **122** 4153–6

[16] Korn T, Heydrich S, Hirmer M, Schmutzler J and Schüller C 2011 *Appl. Phys. Lett.* **99** 102109

[17] Splendiani A, Sun L, Zhang Y, Li T, Kim J, Chim C Y, Galli G and Wang F 2010 *Nano Lett.* **10** 1271–5

[18] Mak K F, He K, Lee C, Lee G H, Hone J, Heinz T F and Shan J 2013 *Nat. Mater.* **12** 207–11

[19] Kumar A and Ahluwalia P 2012 *Eur. J. Phys. B* **85** 1–7

[20] Zhang L and Zunger A 2015 *Nano Lett.* **15** 949–57

[21] Yun W S, Han S W, Hong S C, Kim I G and Lee J D 2012 *Phys. Rev. B* **85** 033305

[22] Chang C H, Fan X, Lin S H and Kuo J L 2013 *Phys. Rev. B* **88** 195420

[23] Yoon Y, Ganapathi K and Salahuddin S 2011 *Nano Lett.* **11** 3768–73

[24] Radisavljevic B, Whitwick M B and Kis A 2011 *ACS Nano* **5** 9934–8

[25] Radisavljevic B, Radenovic A, Brivio J, Giacometti V and Kis A 2011 *Nat. Nanotechol.* **6** 147–50

[26] Wang H, Yu L, Lee Y H, Shi Y, Hsu A, Chin M L, Li L J, Dubey M, Kong J and Palacios T 2012 *Nano Lett.* **12** 4674–80

[27] Kim S *et al* 2012 *Nat. Commun.* **3** 1011

[28] Schwierz F 2010 *Nat. Nanotechnol.* **5** 487–96

[29] Li M O, Esseni D, Snider G, Jena D and Xing H G 2014 *J. Appl. Phys.* **115** 074508

[30] Shi H, Pan H, Zhang Y W and Yakobson B I 2013 *Phys. Rev. B* **87** 155304

[31] Conley H J, Wang B, Ziegler J I, Haglund R F Jr, Pantelides S T and Bolotin K I 2013 *Nano Lett.* **13** 3626–30

[32] Tabatabaei S M, Noei M, Khaliji K, Pourfath M and Fathipour M 2013 *J. Appl. Phys.* **113** 163708

[33] Feng J, Qian X, Huang C W and Li J 2012 *Nat. Photonics* **6** 866–72

[34] Ghorbani-Asl M, Borini S, Kuc A and Heine T 2013 *Phys. Rev. B* **87** 235434

[35] Paussa A and Esseni D 2013 *J. Appl. Phys.* **113** 093702

[36] Fletcher K and Butcher P 1972 *J. Phys. C: Solid State* **5** 212

[37] Soler J M, Artacho E, Gale J D, Garc A, Junquera J, Ordejón P and Sánchez-Portal D 2002 *J. Phys.: Condens. Matter* **14** 2745

[38] Han S *et al* 2011 *Phys. Rev. B* **84** 045409

[39] Lebegue S and Eriksson O 2009 *Phys. Rev. B* **79** 115409

[40] Kaasbjerg K, Thygesen K S and Jacobsen K W 2012 *Phys. Rev. B* **85** 115317

[41] Ataca C and Ciraci S 2011 *J. Phys. Chem. C* **115** 13303–11

[42] Kaasbjerg K, Thygesen K S and Jauho A P 2013 *Phys. Rev. B* **87** 235312

[43] Ma N and Jena D 2014 *Phys. Rev. X* **4** 011043

[44] Li X, Mullen J T, Jin Z, Borysenko K M, Nardelli M B and Kim K W 2013 *Phys. Rev. B* **87** 115418

[45] Ong Z Y and Fischetti M V 2013 *Phys. Rev. B* **88** 045405

[46] Yue Q, Kang J, Shao Z, Zhang X, Chang S, Wang G, Qin S and Li J 2012 *Phys. Lett. A* **376** 1166–70

[47] Esseni D, Palestri P and Selmi L 2011 *Nanoscale MOS Transistors* (Cambridge: Cambridge University Press)

[48] Fischetti M V and Laux S E 1993 *Phys. Rev. B* **48** 2244

[49] Toniutti P, Palestri P, Esseni D, Driussi F, De Michielis M and Selmi L 2012 *J. Appl. Phys.* **112** 034502

[50] Esseni D and Driussi F 2011 *IEEE Tran. Electron Devices* **58** 2415–22

[51] Radisavljevic B and Kis A 2013 *Nat. Mater.* **12** 815–20

[52] Konar A, Fang T and Jena D 2010 *Phys. Rev. B* **82** 115452

[53] Perebeinos V and Avouris P 2010 *Phys. Rev. B* **81** 195442

11